International Journal of Heat and Mass Transfer 164 (2021) 120539

Contents lists available at ScienceDirect

International Journal of Heat and Mass Transfer

journal homepage: www.elsevier.com/locate/hmt

Evaporating hydrophilic and superhydrophobic droplets in electric fields

M.J. Gibbons[a,*], A.I. Garivalis[b], S. O'Shaughnessy[a], P. Di Marco[b], A.J. Robinson[a]

[a] Department of Mechanical and Manufacturing Engineering, Trinity College Dublin, the University of Dublin, Dublin 2, Ireland
[b] DESTEC, University of Pisa, Italy

ARTICLE INFO

Article history:
Received 10 June 2020
Revised 15 September 2020
Accepted 25 September 2020
Available online 23 October 2020

Keywords:
Droplet Evaporation
Electric Field
Hydrophilic
Hydrophobic
Heat transfer
Contact line

ABSTRACT

Evaporating water droplets on a heated substrate are investigated in this work. Specifically, the influences of electric fields are studied in the context of the heat flux distribution beneath the droplets as well as the droplet mechanics and resulting shapes and forces. To facilitate a deeper understanding of the problem, both hydrophilic and superhydrophobic droplets are considered for an entire evaporation period with and without electric field effects. Both wetting scenarios show that the net radial directed electric force is directed inward, resulting in a compressive force which influences the droplet shape in such a way that it appears elongated. Conversely, the net vertically directed electric force is determined to be downwardly directed for hydrophilic droplets, pressing the droplet to the surface, whereas it is upwardly directed for the superhydrophobic droplets, representing a lifting force. With regard to the heat transfer to the droplets, only a pronounced electric field effect was observed for the superhydrophobic droplet. For all droplets, the contact line density, representing the ratio of the contact line perimeter to the total base area of the droplet, is determined to be a parameter that unifies the average heat flux from the heater to the droplets. This suggests that the heat transfer to the base of the droplet in the presence of an electric field is dominated by the electric fields influence, or lack thereof, on the contact line density.

1. Introduction

Phase change phenomena underpin the performance of several engineered systems across a broad spectrum of applications. Control and enhancement of phase change heat transfer can improve performance, efficiency, reliability, and safety. However, smart two-phase systems require an understanding of the fundamental nature of the process. Although significant progress has been made, a full understanding of two-phase systems does not yet exist.

A fundamental phase change process that occurs in nature as well as in engineering systems is sessile droplet evaporation upon heated surfaces. Droplet evaporation is a complex interaction of diffusion within the substrate, buoyant convection in the gas and liquid phases, contact line evaporation, vapour diffusion, evaporative cooling at the liquid-gas interface and possible Marangoni effects [1–10]. Albeit a proportionately small region compared with the overall droplet size, the heat and mass transfer at the contact line has been shown to be an important factor in droplet evaporation [1–3,10,11].

Droplet evaporation can be categorised into four regimes: constant contact angle (CCA), constant contact radius (CCR), mixed, and stick-slip. The evaporation regime is primarily dictated by the wetting characteristics between the liquid and the surface, with CCA mode being associated with hydrophobic droplets and CCR being associated with hydrophilic droplets. The characteristic difference between a hydrophilic and hydrophobic droplet, and thus their evaporation dynamics, is in the formation of their respective contact lines (see Fig. 1). Interestingly, however, in both cases, the peak heat transfer has been shown to occur at their respective contact lines [1,2,11]. For a hydrophilic droplet, the adsorbed film region forms due to the strong long-range intermolecular forces between the solid and liquid phases. These forces result in a transition micro-region of low thermal resistance in the region of the contact line [3]. For the hydrophobic case, the contact line structure is distinctly different due to the weak adhesion forces between the liquid and solid phases. This results in a considerably smaller adsorbed film region [12], which prevents the creation of a transition micro-region region, as illustrated in Fig. 1b. At the contact line of a hydrophobic droplet, the thermal boundary layer within the heated droplet intersects the liquid-gas interface creating a region below which the liquid-gas surface temperature is high. At this location, diffusion and possibly advection of heat to

* Corresponding author
E-mail address: Michael.Gibbons@tcd.ie (M.J. Gibbons).

https://doi.org/10.1016/j.ijheatmasstransfer.2020.120539
0017-9310/

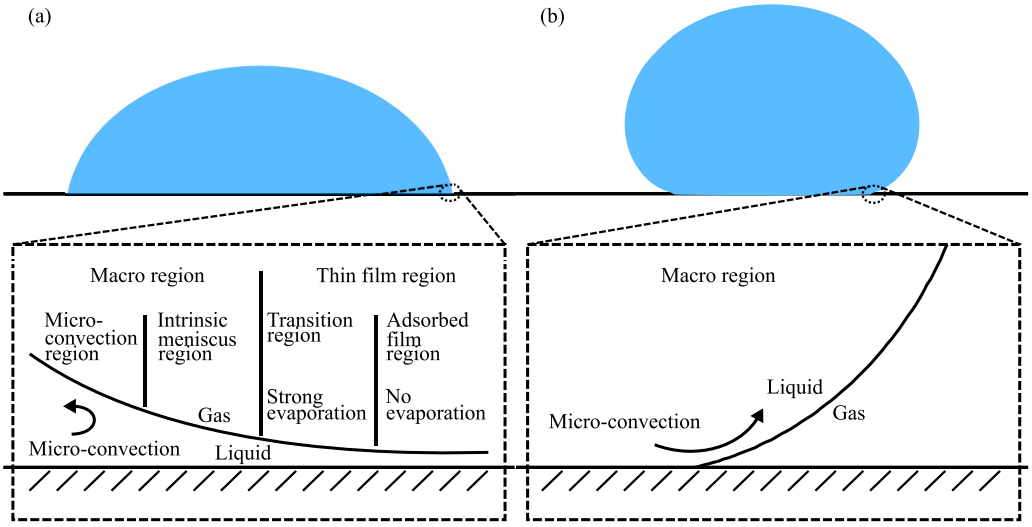

Fig. 1. Evaporation at the contact line. (a) partially wetting droplet and (b) partially non-wetting droplet.

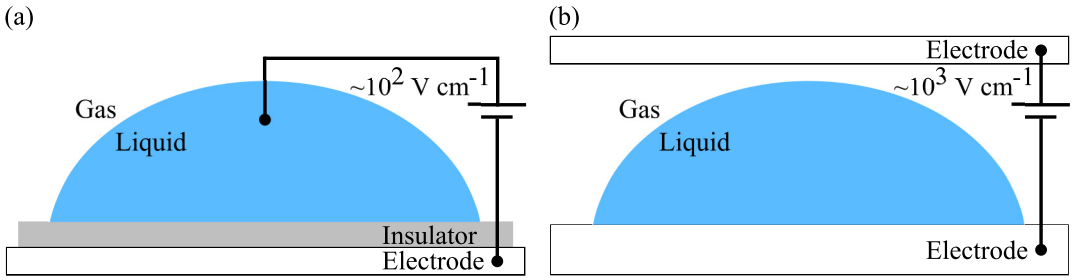

Fig. 2. Schematic of the electrode configuration. (a) The electric field is established inside the drop. The upper electrode is in contact with the drop volume. (b) The electric field is established outside the drop. Adapted from Vancauwenberghe et al. [9].

the droplet interface is released effectively, due to the proportionately high saturation pressure [2]. Therefore, the proximity of the heated surface and the liquid-gas interface at the contact line region combined with the high vapour diffusion to the ambient creates an overall lower thermal resistance pathway between the heat source (heated substrate) and the heat sink (the ambient air). It has been shown in the literature that when an ambient temperature water droplet is placed on a heated substrate, Marangoni convection initially dominates due to the temperature gradient from the base of the droplet to the droplet apex. This surface tension driven flow homogenises the droplet temperature subsequently reducing the thermal Marangoni flow [13]. Thereafter, heat transfer within the bulk liquid of both droplet types can be dominated by convection or conduction depending on the magnitude of the Peclet number [14,15]. Transferred thermal energy from the substrate to the droplet base can be dissipated by four pathways: sensible heating of the droplet, latent heat through phase change of the fluid, gas convection on the liquid-gas interface from surrounding conditions and radiation [13]. In the case of a relatively small diameter droplet on a large heated substrate, it has been shown that free air convection is formed over the hot wall and accelerates the droplet evaporation by 20–30% [13,16].

Heat and mass transfer augmentation using an electric field is of scientific and engineering interest due to its capability of enhancing and controlling two-phase processes and doing so with low energy consumption [9]. The use of an electric field has applications in numerous fields, including heat and mass transfer [9,17–21], particle manipulation [22], coating [23], and drying [24]. Notably, the application of a static electric field has been shown to change the morphology, contact angle, and wetted area of a sessile droplet [10,25–29]. Although the enhancement of heat transfer by application of an electric field is well documented in scenarios such as boiling and condensation [19,30–32], its influence on evaporating droplet dynamics is an underdeveloped topic. Two primary electrode configurations have been implemented in the literature in characterising the impact of a static electric field on an evaporating droplet. These are depicted in Fig. 2. In the first case, as shown in Fig. 2a, one of the electrodes is placed in contact with the droplet, creating an electric field inside the droplet. In the second configuration (Fig. 2b), the electric field is established between two plate electrodes. This setup requires an order of magnitude greater voltage potential compared to the first orientation [9].

Takano et al. [33–36] investigated the impact of a static electric field on the evaporation of a droplet on a substrate above the Leidenfrost point, using the electrode configuration shown in Fig. 2a. In their first study [33], for an applied voltage of 300 V, they reported an evaporation time enhancement of ~3 × for water, ~20 × for ethanol, and ~1.3 × for cyclohexane in comparison with the non-electric field case. In a subsequent study [34], by applying a maximum voltage of 250 V and 2000 V for ethanol and R113, respectively, peak evaporation time enhancements of 7.6 × and 2.8 × were demonstrated.

Vancauwenberghe et al. [9] reviewed droplet mechanics and the influence of electrostatic forces on the droplet shape, including the contact angle. It was found that the droplet shape becomes elongated in the presence of an electric field due to radial orientated compressive electrostatic forces. For a hydrophilic droplet, the net resultant vertical electrical force was directed downward, thus pushing the droplet to the surface.

Gibbons et al. [10] investigated the local heat flux distribution to an evaporating 80 μL hydrophilic water droplet on a heated 25

μm thick stainless steel substrate for varied static electric fields. Four electric field strengths were characterised using the two-electrode configuration shown in Fig. 2b: 0 kV cm^{-1}, 5 kV cm^{-1}, 10 kV cm^{-1}, and 11 kV cm^{-1}. Despite the clear change in the droplet morphology and contact angle due to the electric field, no distinct change in the radial heat flux distribution across the solid-liquid boundary was noted.

Almohammadi and Amirfazli [37] explored diffusion-limited evaporation of a 20 μL sessile water droplet on four substrates with and without a static electric field. The four substrates characterised were aluminium, PEMA, PS, and Teflon for electric field strengths approaching the electric breakdown of air. They noted an increase in the total evaporation time for the electric field case in comparison to the non-electric field except for a surface with considerable contact angle hysteresis (CAH).

Droplet evaporation on a heated substrate is a complex multi-physics phenomenon. While considerable progress has been made in the recent past to elucidate the conjugate heat transfer near the triple contact line [1–3], droplet evaporation in an electric field still requires significant research to understand the problem completely. Previous work by the present authors [1,2] investigated the local heat flux distribution beneath evaporating hydrophilic and superhydrophobic water droplets using thermal imaging and geometric analyses in the absence of an electric field. The current investigation extends upon this earlier work by exploring the spatial distribution of the surface heat flux beneath an evaporating hydrophilic and superhydrophobic droplet in a static electric field over its complete life-cycle and compares it to that of the previously characterised non-electric field cases. To the authors' knowledge, this study is the first to compare the local heat transfer beneath both partially wetting and non-wetting evaporating droplets for a full evaporation event in static electric fields. Simultaneously, the droplet interfaces are experimentally and numerically analysed and contrasted to investigate the impact of the electric field on geometric properties and subsequent heat transfer and droplet mechanics.

2. Experiment and analysis

2.1. Experimental apparatus

The experimental facility is shown in Fig. 3. The experimental facility, data reduction, and analysis have been described in detail in previous work published by the present authors [1,2]. Therefore, only a brief description will be given here. An 80 μL water droplet is deposited on the substrate at the start of testing. The substrate

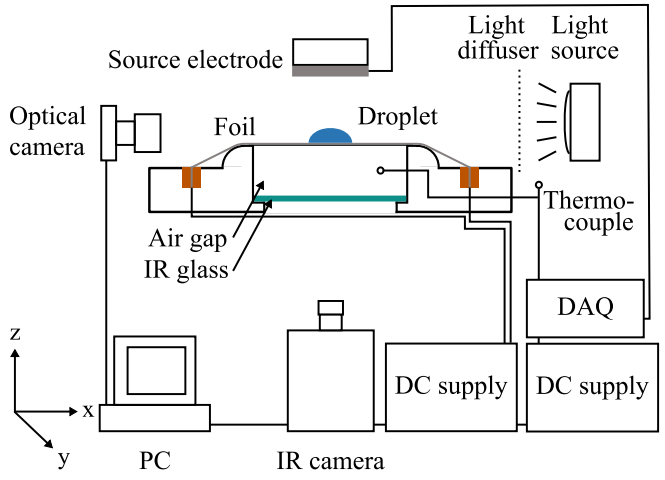

Fig. 3. Schematic of the experimental apparatus.

Table 1
Foil and paint properties.

	Foil	Paint
Thickness, δ [μm]	25	10.52
Density, ρ [kg m^{-3}]	7960	1261
Thermal conductivity, k [W m^{-1} K^{-1}]	16.3	0.095
Specific heat, C_p [J kg^{-1} K^{-1}]	502	2835
Roughness uncoated, Ra_u [nm]	60	-
Roughness coated, Ra_c [nm]	176	-
Paint emissivity, ε_p [-]	-	0.95

is 25 μm thick 316 stainless steel foil (Goodfellow, 140 mm × 80 mm × 0.025 mm, P/N: 505-400- 04). Two surface wetting conditions are explored during testing; hydrophilic and superhydrophobic. A hydrophilic wetting condition ($\theta_A = 85^\circ$, $\theta_R = 55^\circ$) is obtained for the raw, contaminant-free, stainless steel foil. The superhydrophobic wetting case ($\theta_A = 155^\circ$, $\theta_R = 150^\circ$) is achieved using Glaco Mirror Coat Zero [2]. The thermal resistance and thickness of the superhydrophobic coating are assumed negligible during analysis. The underside of the foil is coated with a 10.5 μm thick layer of matte black paint to provide a known, high emissivity surface for infrared thermography. The substrate properties are outlined in Table 1 [21]. During testing, the substrate is uniformly heated by the Joule effect establishing a surface heat flux of 912 W m^{-2} and a substrate temperature of ~70°C at a steady state when no droplet is present. The temperature through the thickness of the foil and paint layers is assumed constant due to the low calculated Biot numbers ($Bi \ll 1$).

The electric field is established between the stainless-steel foil and a high potential stainless-steel flat disc electrode that is placed directly above the droplet during experimentation, as per Fig. 2b. This electrode is 5 mm in thickness and 55 mm in diameter. It is maintained at a 10 mm separation height from the foil for all tests. In this setup, the foil acts as a pseudo ground due to its relatively low potential compared with the disc electrode.

The droplet morphology is captured using an optical camera (Point Grey, P/N: CMLN-1352M) fitted with a microscopic lens and extension tube (Infinity Proximity, P/N: 57-724 and 39-686) that is mounted parallel to the steel foil. It has a resolution of 1280 × 960 pixels with a pixel size of 10.5 μm. A multiple LED light (GS Vitec MultiLED, P/N: GS 01372) is used to illuminate the droplet. The temperature distribution from the heated substrate to the solid-liquid interface of the droplet is captured using a thermal imaging camera (FLIR, NETD: <20 mK, P/N: SC6000) fitted with a 25 mm focal length lens. The IR camera is mounted beneath the substrate and is focused on the underside of the heated foil. During testing, the thermal imaging camera records at a resolution of 400 × 400 pixels, with a pixel size of 160 μm.

The substrate heat flux, optical camera, and thermal imaging camera are all automated using a custom-built LabVIEW program. Thermal data is acquired for 1 s every 60 s at 400 Hz. The optical camera is set to record at 2 Hz throughout the evaporation period.

To calculate the heat flux distribution, an element-wise energy balance, shown in Fig. 4, is applied to the captured thermal image. Each element consists of a volume $dx \times dx \times \delta$, where dx is the pixel width of the IR camera and δ is the thickness of the substrate. Uniform heat generation across the foil and paint layers is assumed. A lumped capacitance analysis is preformed as Bi $\ll$ 1 for both the foil and paint layers. Accounting for system losses, conjugate heat transfer (lateral conduction), and energy storage within the substrate yields:

$$q''_{con} = q''_{gen} - q''_{cond} - q''_{rad,b} + \left(k_f\delta_f + k_p\delta_p\right)\left(\frac{\partial^2 T_s}{\partial x^2} + \frac{\partial^2 T_s}{\partial y^2}\right) - \left(\rho_f C_{p,f}\delta_f + \rho_p C_{p,p}\delta_p\right)\frac{\partial T_s}{\partial t} \quad (1)$$

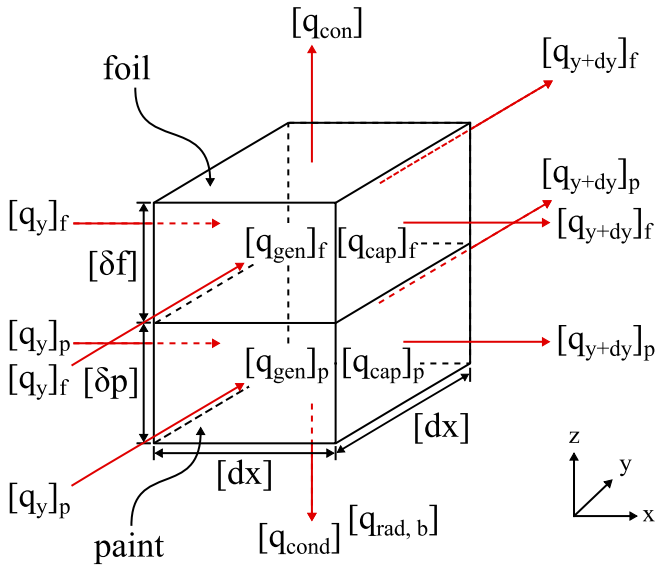

Fig. 4. Heated substrate energy flow balance within a single dx × dx element of thickness δ_f and δ_p.

Table 2
Heat transfer experimental uncertainty.

	[W/m^2]	[%]
q''_{gen}	± 2.2	± 0.26
q''_{cond}	± 0.7	± 0.32
$q''_{rad,b}$	± 0.3	± 0.29
q''_{lc}	± 524.6	± 21.32
q''_{cap}	± 1.5	± 11.24
q''_{con}	± 526.5	± 16.07

where k_f, k_p, δ_f, δ_p, $C_{p,f}$, and $C_{p,p}$ are the foil and paint thermal conductivity, thickness, and specific heat capacity, respectively. The values for these parameters are shown in Table 1. Eq. (1) accounts for the generated flux within the metal substrate (q''_{gen}), the one-dimensional conduction (q''_{cond}) and the radiation ($q''_{rad,b}$) through the 7 mm air gap from the underside of the substrate. The final two terms in Eq. 1 are the heat transfer due to lateral conduction (q''_{lc}) and heat storage (q''_{cap}) within the substrate, respectively. q''_{con} is the heat flux transferred from the heated substrate into the evaporating droplet. q''_{con} also encompasses the heat flux into the surrounding air in the far-field ($S_r \gg R_b$). The droplet evaporation is assumed quasi-steady during the 1 s capture period. This approximation is correct due to the proportionately small calculated energy storage term for all test points. The radial profile of the heat flux is determined by averaging lines taken radially from the centre of the droplet at 0.5° increments.

The experimental uncertainty for the terms in Eq. 1 is shown in Table 2 [38]. All listed values are to a 95% confidence level. A combined uncertainty approach is then applied on a pixel by pixel basis.

3. Results and Discussion

3.1. Electric field augmentation

The shape of a droplet at equilibrium in an electric field is a balance between the surface tension, buoyancy, internal pressure and the electric field forces. Where the surface tension acts to make the droplet spherical, gravity flattens it, and the electric field tends to elongate the drop along the field direction [9]. The interface profile of the evaporating droplets is determined from the captured optical images. The interface profiles of a hydrophilic droplet and a superhydrophobic droplet with and without an applied static electric field are shown in Fig. 5a and b, respectively. The magnitude of the applied static electric fields corresponds to that approaching electrical breakdown at t = 0 min for both cases. Fig. 5a and b demonstrate the impact of the static electric field on the droplets' morphology for similar volumes at t = 1 min. For both wettability scenarios tested (Fig. 5a and b), the electric field acts to increase the droplet height (H_d) by 18% and 27% for the hydrophilic and superhydrophobic, respectively. For the hydrophilic case (Fig. 5a), the apparent contact angle (θ) is reduced from 80° to 74°, while for the superhydrophobic case (Fig. 5b), the applied electric field acts to decrease the droplet base diameter from 2.1 mm to 1.5 mm. This change in the droplet base radius can be attributed to the low contact angle hysteresis ($\theta_{CAH} = 5°$) of the superhydrophobic wetting condition. When the electric field is applied, the droplet contact angle decreases for the superhydrophobic case. Once the contact angle is reduced below the receding contact angle of the droplet, the contact line unpins and recedes, thus reducing the droplet base radius (R_b). No reduction of the base radius of the hydrophilic case is noted due to the relatively large contact angle hysteresis ($\theta_{CAH} = 35°$) of the hydrophilic wetting condition. These results are consistent with that reported previously in the literature [10,37].

Fig. 5c and d shows the influence of the applied electric field on the radial heat transfer profile (q''_{con}) to the base of the droplets for the interface profiles discussed in Fig. 5a and b.

For all radial heat flux profiles investigated in Fig. 5c and d, the peak local heat transfer is noted at the contact line. This is due to the low thermal resistance at the contact line and is consistent with previous studies [1,2,10,21]. For the hydrophilic case (Fig. 5c), the presence of an 11 kV cm^{-1} electric field appears to have an insignificant influence on the radial heat transfer profile despite an increase in the droplet height and a reduction of the apparent contact angle. This is consistent with the results of Gibbons et al. [1] who observed, in the absence of an electric field, that the heat flux distribution to the base of the droplet was found to be insensitive to the droplet geometric properties (contact angle, droplet height, liquid-gas surface area, and volume), for a similar base radius and contact line length. The results here for the case of an electric field provides corroborating evidence to support the hypothesis that the heat transfer to the liquid in the bulk as well as in the contact line region is insensitive to the droplet size and morphology.

In the superhydrophobic case, Fig. 5d shows that the electric field acts to increase the droplet height and decrease the droplet base radius. In contrast to the hydrophilic droplet, the heat flux profile at the base of the droplet notably changes. As will be discussed, it is hypothesised that the increase in peak and average heat flux in the presence of the electric field is related to the action of the electric field on the overall shape of the droplet which results in an increase in the contact line density due to the decreased base radius, as opposed to specific electric field effects on the heat transfer mechanisms near the wall.

3.2. Droplet Morphology

From the droplet interface and assuming axisymmetry, a number of important geometric parameters can be determined. Some of these parameters are illustrated in Fig. 6a, where θ is the droplet contact angle, V_d is the droplet volume, H_d is the droplet height, and D_b is the droplet base diameter. Fig. 7 contrasts these geometric properties of the hydrophilic and superhydropho-

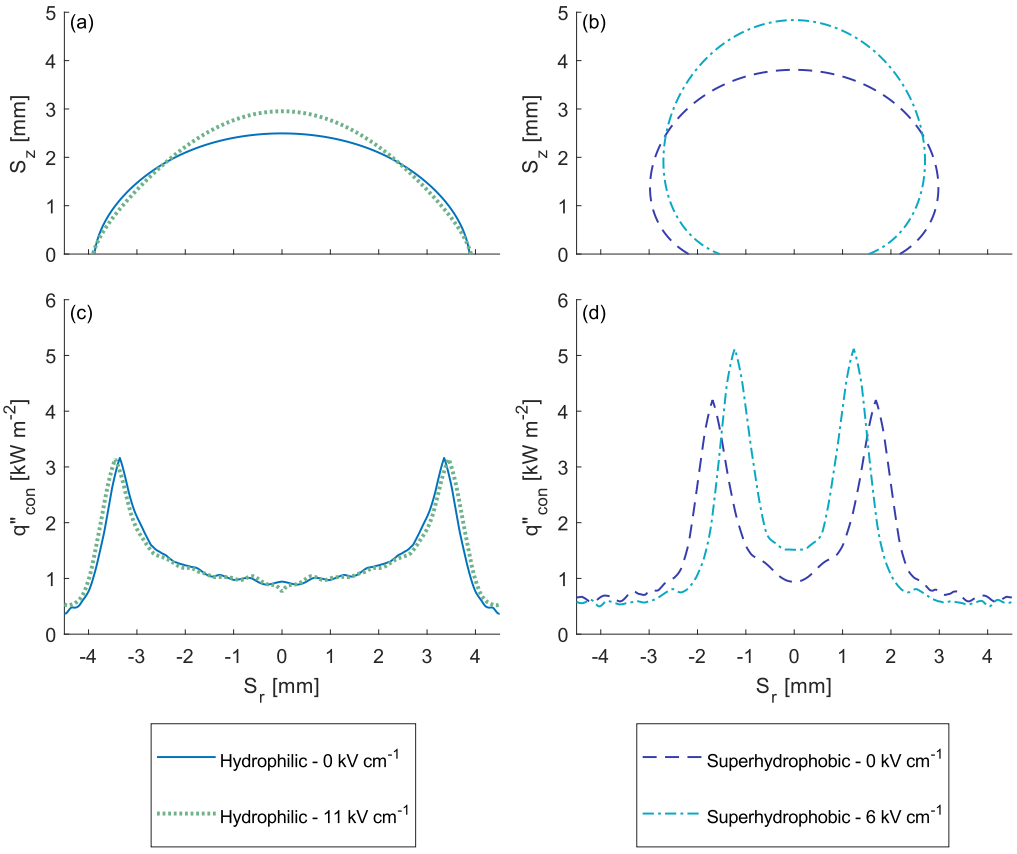

Fig. 5. Droplet liquid-gas interface profiles and radial heat flux profiles for similar droplet volume and varied applied electric fields at t = 1 min. (a)&(c) hydrophilic and (b)&(d) superhydrophobic.

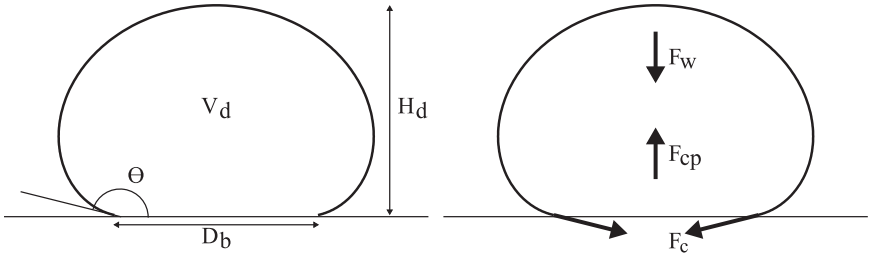

Fig. 6. Schematic of droplet (a) geometric parameters and (b) bulk force analysis.

bic droplets in varied electric field conditions throughout their evaporation periods.

In the absence of an electric field, the hydrophilic droplet initially evaporates with a constant contact radius (t = 0-9 min, R_b= 3.9 mm), indicating CCR evaporation mode. Approximately halfway through its evaporation period, the droplet contact angle decreases to below that of the receding contact angle ($\theta_R = 55^\circ$) causing the contact line to unpin and hereafter recede. After this event, the droplet evaporates alternating between a constant contact angle mode (t = 9-11 min and t = 15-21 min) and mixed-mode (t = 12-14 min). The hydrophilic droplet in the electric field follows a similar trend, though with some notable differences. The droplet evaporates initially in CCR mode (Fig. 7e, t = 0-6 min, R_b= 3.9 mm) but transitions to the CCA mode earlier compared to its non-electric field counterpart. As Fig. 7c shows, the electric field acts to reduce the apparent contact angle. It thus reaches the receding contact angle earlier than its non-electric field counterpart, resulting in earlier unpinning of the droplet contact line. The droplet then evaporates in a sustained CCA regime (Fig. 7c, t = 7-17 min, $\theta = 55^\circ$) before switching to the mixed-mode (t = 18-21 min) for the remainder of the evaporation process. It is interesting to note that both hydrophilic droplets take a similar amount of time to achieve complete evaporation, with the electric field case completing its evaporation in marginally less time (30 s), which is within the repeatability of the experiments. This will be discussed in more detail later.

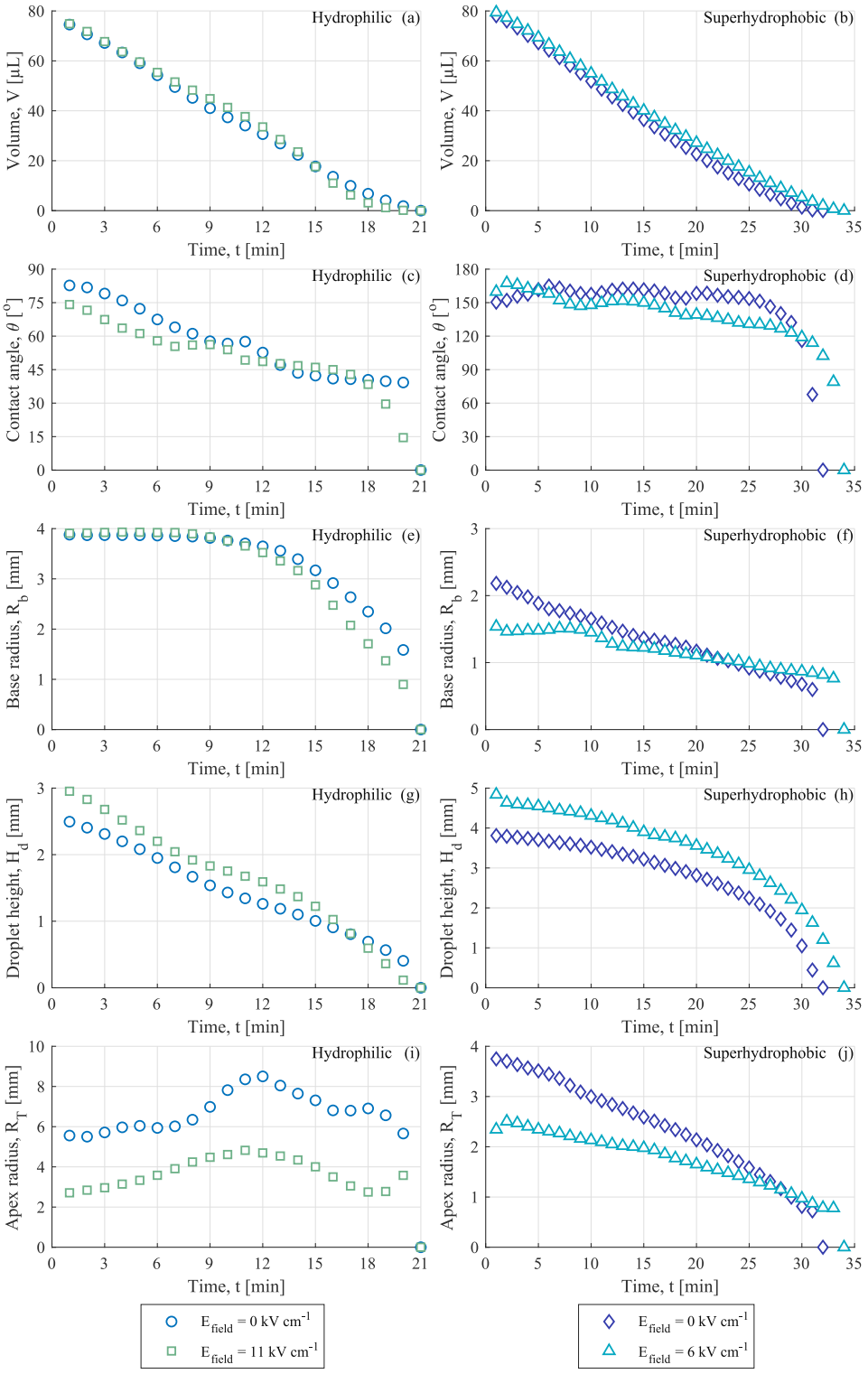

Fig. 7. Hydrophilic and superhydrophobic droplet geometric properties through time for varied applied electric field. (a-b) volume, (c-d) contact angle, (e-f) base radius, (g-h) height, and (i-j) apex principal radii.

In the absence of the electric field, the superhydrophobic droplet evaporated predominantly in CCA mode. A consistent contact angle of $\theta \approx 150^{\circ}$ is noted between t = 1-28 min, with a receding contact line and decreasing droplet height (Fig. 7d, f, and h). In the presence of the electric field, the superhydrophobic droplet evaporates initially in the CCR regime (t = 1-9 min), before transitioning to a CCA regime (t = 10-16 min, $\theta = 150^{\circ}$). Finally, the droplet completes its evaporation in the mixed-mode (t = 17-34 min). For the test conditions considered here, the electric field acts to increase the total droplet evaporation time marginally (t_e = 34 min) in comparison to the non-electric field case (t_e = 32 min).

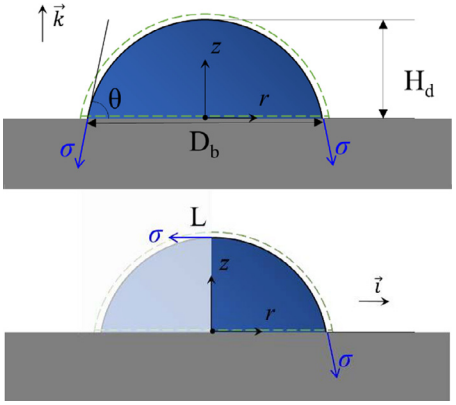

Fig. 8. System and geometrical properties definition for the two force balances. (a) vertical balance along unit vector *k*, (b) radial balance along unit vector ***i***.

3.3. Droplet Mechanics

Using the droplet height (H_d), volume and apex curvature (R_T) it is possible to calculate the droplet interface profile using the Young-Laplace equation for the hydrostatic non-electric field cases [9,39]. This is expressed as;

$$\sigma\left(\frac{1}{R_1}+\frac{1}{R_2}\right)=\frac{2\gamma}{R_T}-g(\rho_l-\rho_g)(z-H_d) \tag{2}$$

where R_1 and R_2 are the principal radii of curvature at any point on the interface, R_T is the radius of the droplet apex, σ is the surface tension, ρ_l and ρ_g are the density of the liquid and surrounding gas respectively, H_d and z are the droplet height and the height of the point on the interface being evaluated respectively. Gibbons et al. [1] previously showed agreement between the analytical and measured droplet profiles. Integration of the Young-Laplace equation from the tip to the base of a droplet gives the acting net vertical forces acting upon the droplet in mechanical equilibrium.

The balance of vertical forces acting on the droplets considered here during their entire evaporation period are shown in Fig. 6b. These forces are the buoyancy force (F_w), the capillary force (F_C), the contact pressure force (F_{cp}), defined by Eqs. 3-5.

$$F_w=-V(\rho_l-\rho_g)g\,\boldsymbol{k} \tag{3}$$

$$F_c=-D_b\pi\sigma\sin\theta\;\boldsymbol{k} \tag{4}$$

$$F_{cp}=\frac{\pi {D_b}^2}{4}\left(\frac{2\sigma}{R_T}+(\rho_l-\rho_g)gH_d\right)\boldsymbol{k} \tag{5}$$

The forces acting in the radial direction can be calculated as well: no buoyancy force acts in the radial direction, so the forces are just the capillary force ($F_{C,R}$) and the pressure force ($F_{cp,R}$), The expressions defined by Eqs. 6-7 are derived considering the equilibrium of half droplet, cut along the meridian and the base diameter (L is the liquid-vapour interface length along the meridian): This is shown in Fig. 8.

$$F_{c,R}=-\sigma(L-D_b\cos\theta)\boldsymbol{i} \tag{6}$$

$$F_{cp,R}=\left[\int_0^{H_d}\int_0^{r(z)}\left(\frac{2\sigma}{R_T}+(\rho_l-\rho_g)g\right)drdz\right]\boldsymbol{i} \tag{7}$$

To satisfy mechanical equilibrium with no electric field in both vertical and radial directions, $\sum F=F_{net}=0$. The field-free scenarios are depicted in Figs. 9a-d for both the hydrophilic and superhydrophobic droplets, and both the measured droplet profiles and the Young-Laplace solution are shown for comparison. For both cases, a near-zero net force is noted for all points, and trends and magnitudes similar to the Young-Laplace analysis are observed. Non-zero discrepancies are attributed to experimental uncertainty related to measuring of the contact line of an evaporating droplet (*e.g.* droplet reflections, shadowing, and the mirage effect). The propagation of errors for the calculated geometric values and forces acting on the droplets are provided in Table 3.

Table 3
Experimental measurement error and uncertainty.

Parameter		PU [%]
Droplet volume, V_d	±	2.4
Contact angle, θ	±	11.1
Base diameter, D_b	±	3.1
Droplet height, H_d	±	0.8
Apex radius, R_T	±	12.9
Buoyancy force, F_w	±	11.0
Capillary force, F_c	±	3.2
Pressure force, F_p	±	10.5
Electrical force, F_e	±	29.4

The most noticeable difference between the field-free hydrophilic and superhydrophobic droplets considered here is the magnitude of the forces. Although the buoyancy forces are of commensurate magnitude, owing to their initial volumes being the same and similar evaporation rates, the capillary and contact pressure forces for the hydrophilic droplet are notably larger than that of the superhydrophobic droplet owing to its larger base radius and associated contact area. Because of this, the relative magnitudes of the forces are also different. The hydrophilic droplet is primarily a balance of contact pressure and capillary forces. In contrast, the superhydrophobic droplet is mainly a balance between the contact pressure and the buoyancy force.

As Fig. 5 illustrated the electrostatic forces acting on the droplets can alter their shapes. This change in shape over the contour of the droplet is indicative of the net influence of the additional electric stresses acting locally over the interface profile. In short, the additional local electric stress changes the local equilibrium stress balance in such a way that the radii of curvature change in order to re-establish local mechanical equilibrium. The net effect over the entire interface is an overall change in the shape of the droplet due to local curvatures adjusting to different magnitudes of the local electric stress.

Considering the force balances, a droplet placed in an electric field must include the cumulative effect of the distributed electric stress on the interface such that an additional electric force (F_e) is involved in establishing mechanical equilibrium such that:

$$|F_{cp}|-|F_w|-|F_c|+F_e=0 \tag{8}$$

$$\left|F_{p,R}\right|-|F_{c,R}|+F_{e,R}=0 \tag{9}$$

Eqs. 8 and 9 make it possible to evaluate experimentally the resulting vertical and radial electric forces, once the other involved forces have been determined from the profile by Eqs. 3-7. As described by Di Marco [40], the electric force F_e in the vertical direction can be evaluated as the sum of three terms: $F_{e,S}$ that is the force acting on the liquid-vapor interface, $F_{e,A}$ that is the force acting on the liquid-solid interface, and $F_{e,p}$ that is the contribute of the internal pressure of the droplet:

$$F_e=F_{e,S}+F_{e,A}+F_{e,p} \tag{10}$$

More details on the three terms of the electric force are given in Appendix A.

Fig. 9e and 9f plot the vertical force balance histories of the hydrophilic and superhydrophobic droplets in the presence of an

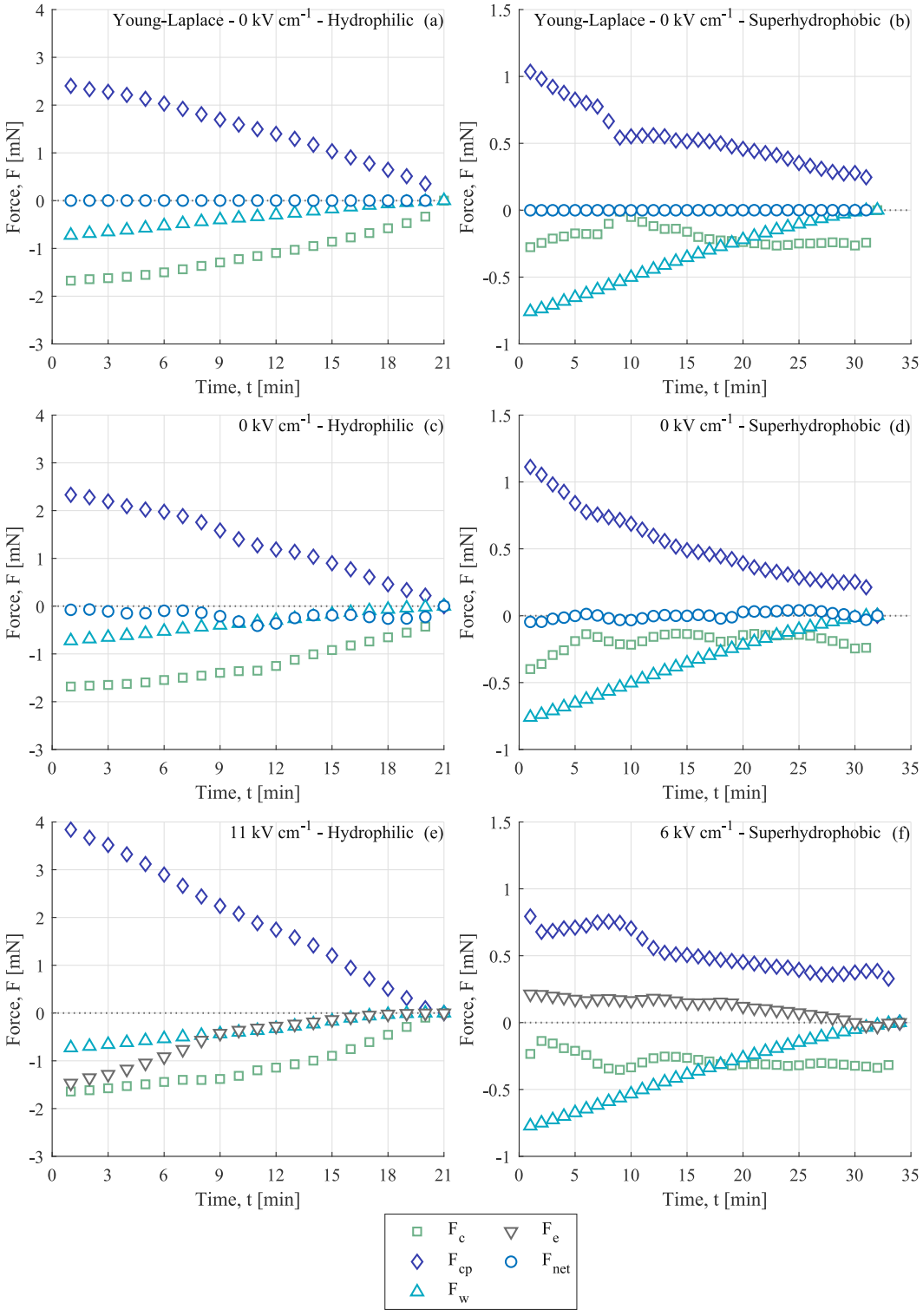

Fig. 9. Droplet vertical force analysis. (a) hydrophilic - Young-Laplace, (b) superhydrophobic - Young-Laplace, (c) hydrophilic - 0 kV cm^{-1}, (d) superhydrophobic - 0 kV cm^{-1}, (e) hydrophilic - 11 kV cm^{-1}, and (f) superhydrophobic - 6 kV cm^{-1}.

electric field. For the hydrophilic case, Fig. 9e shows a net downward directed electric force for the majority of the evaporation period, in essence pressing the droplet to the surface.

Fig. 10a and b show the radial force balance of the hydrophilic and superhydrophobic droplets during their evaporation lifespan, respectively. For the hydrophilic droplet, (Fig. 10a) during the initial time interval, when the droplet is pinned, it is clear that the net radial force is directed inward and diminishes in magnitude to near zero as the volume and height reduce. For the superhydrophobic case (Fig. 10b), a net inward radial force that decreases in magnitude is also observed over the course of the evaporation.

Comparing the electrical vertical (Fig. 9e and f) and radial (Fig. 10a and b) forces, it can be said that for the hydrophilic case

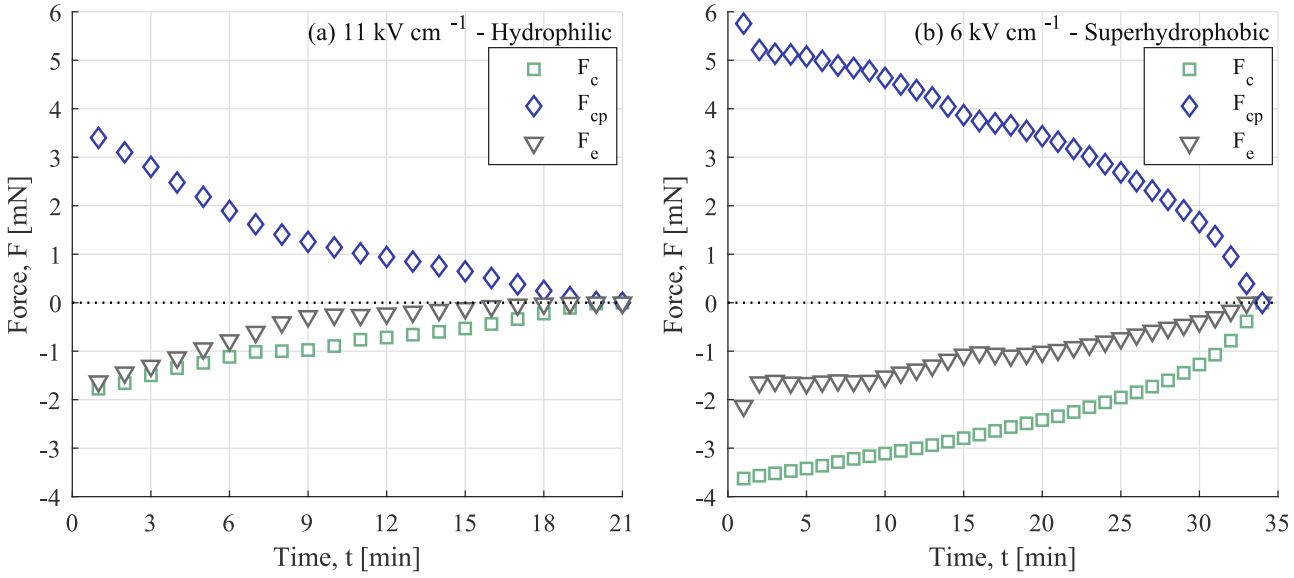

Fig. 10. Droplet electric field radial force analysis. (a) hydrophilic - 11 kV cm^{-1}, and (b) superhydrophobic - 6 kV cm^{-1}.

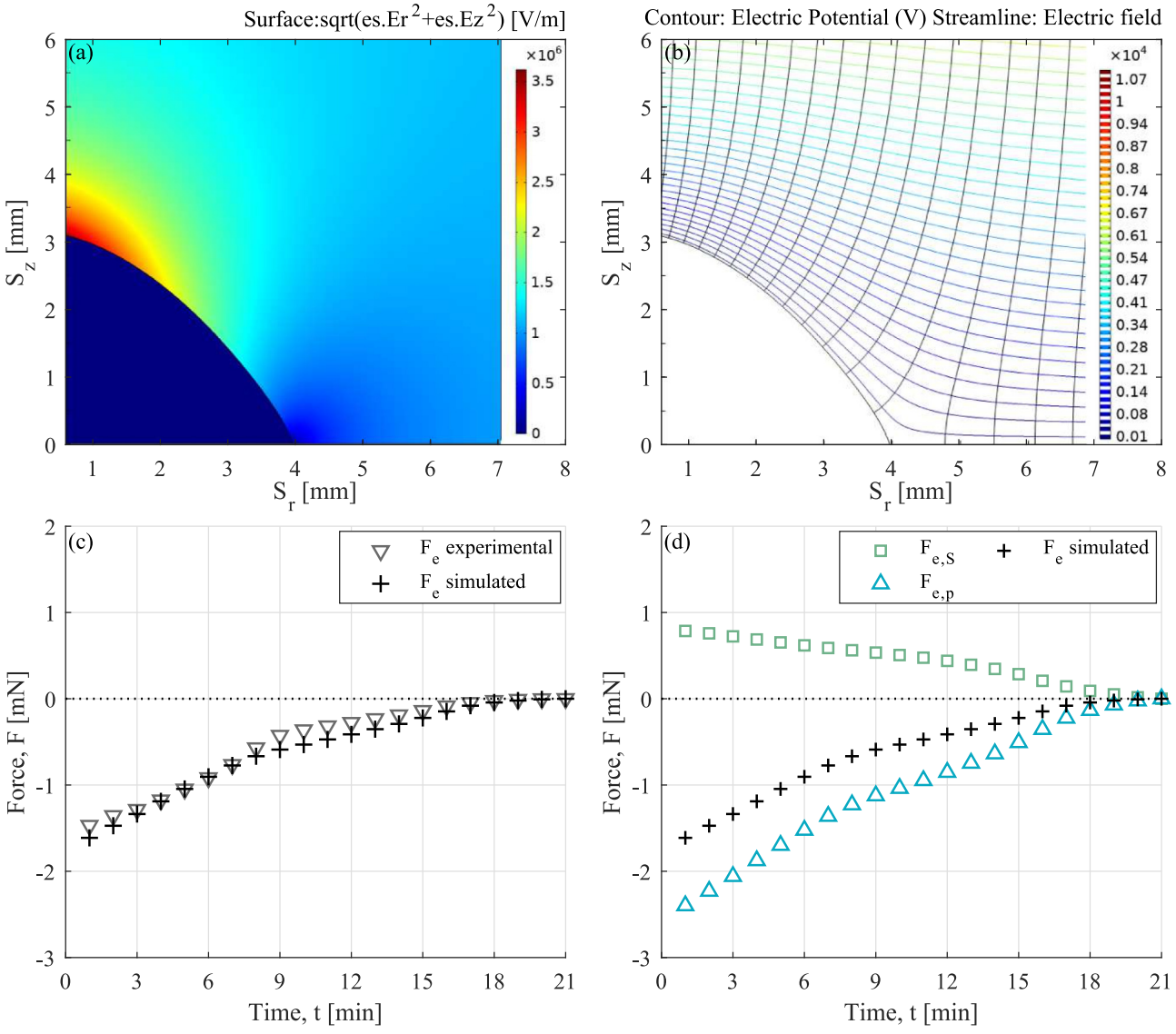

Fig. 11. (a) Droplet profile and electric field distribution for the hydrophilic droplet with applied electric field strength of 11 kV cm^{-1}, (b) simulated electric potential and electric field lines for the hydrophilic droplet with applied electric field strength of 11 kV cm^{-1}., (c) simulated and experimental net vertical force, and (d) electric force components for the hydrophilic droplet with applied electric field strength of 11 kV cm^{-1}.

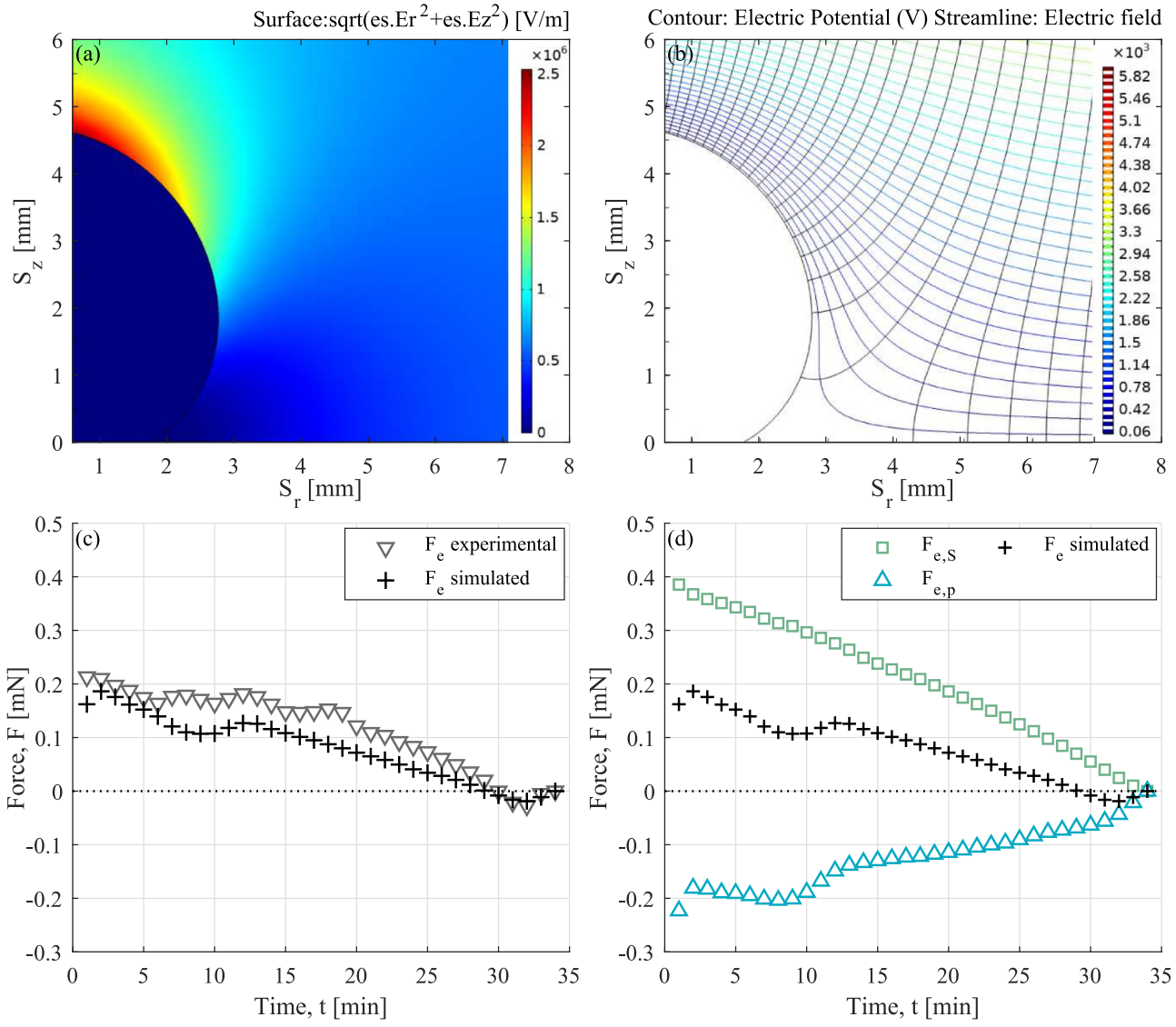

Fig. 12. (a) Droplet profile and electric field distribution for the superhydrophobic droplet with applied electric field strength of 6 kV cm^{-1}, (b) simulated electric potential and electric field lines for the hydrophilic droplet with applied electric field strength of 6 kV cm^{-1}., (c) simulated and experimental net vertical force, and (d) electric force components for the superhydrophobic droplet with applied electric field strength of 6 kV cm^{-1}.

the electrical force compresses the droplet inward and downward, while for the superhydrophobic case the electric force acts to compress the droplet inward and upward.

To better understand the action of the induced electric field forces, numerical simulations were performed using COMSOL multi-physics in order to estimate the electric field distribution and theoretically estimate the local electric stresses and net vertical electric forces. The liquid is set to electrically conducting. The numerical simulations are detailed in Appendix A.

Fig. 11a and b show the calculated electric field distribution and electric potential in the vicinity of the droplet for t = 1 minute. It can be noted that, as the liquid has been considered a conductor, the electric field is totally excluded in the liquid region. Fig. 11c shows that the electrical force calculated with the simulation is in good agreement in magnitude and directionality with the experimentally determined force. Fig. 11d gives deeper insight into the nature of the electric force: the force $F_{e,A}$ acting on the liquid-solid interface is null in this case and not included. The term $F_{e,S}$ acting on the liquid-vapour phase pulls the droplet upwards, while $F_{e,p}$ gives a negative contribution that overcomes the former one.

In summary, it can be said that for the hydrophilic droplet considered here, the main influence is observed in the early stage of the evaporation period, where there is sufficient volume of liquid penetrating into the electric field to cause the electric field gradients to be sufficient to influence the overall shape and resulting forces. Here the main influence is a pressing of the droplet onto the surface vertically and a net radial inward compression of the droplet.

For the superhydrophobic case, Fig. 9f shows a net upwardly directed electric force for the majority of the lifespan of the droplet, in essence lifting the droplet from the surface. The magnitude of the electric force is similar to that of the capillary force. Yet, here it is in the opposite direction compared with the hydrophilic droplet. The additional electric force in this scenario is balanced by a decrease in the contact pressure force, here brought about by a reduction in the base radius and associated contact area. Commensurate with the observations for the hydrophilic droplet, the magnitude of the net vertical electric force decreases with time as the droplet volume and height decrease, to the point of becoming diminishingly small near the end of its evaporation period. Fig. 12a

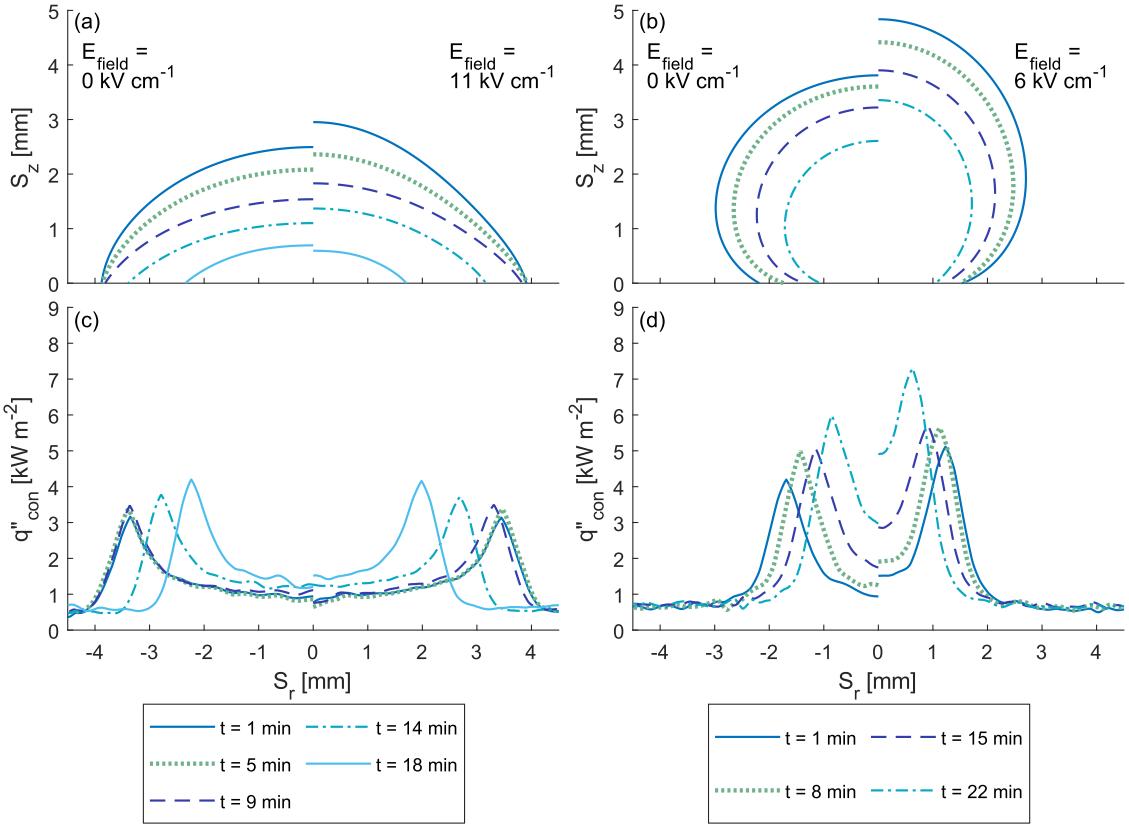

Fig. 13. Droplet profile and radial heat transfer profile for varied wetting and applied electric field conditions. (a) hydrophilic 0 kV cm^{-1} (left) and 11 kV cm^{-1} (right), (b) superhydrophobic 0 kV cm^{-1} (left) and 6 kV cm^{-1} (right), (c) hydrophilic 0 kV cm^{-1} (left) and 11 kV cm^{-1} (right) radial heat transfer profile, and (d) superhydrophobic 0 kV cm^{-1} (left) and hydrophilic 11 kV cm^{-1} (right) radial heat transfer profile.

and b show the simulated electric field distribution and electric potential in the vicinity of the droplet for t = 1 minute. Fig. 12c shows the simulated vertical force balance, which is in good agreement with the experimentally determined ones shown in Fig 9f, thus verifying their correctness. Compared with the hydrophilic case, there are important differences in the electric force terms (Fig. 12d): this time, the two non-zero terms are comparable. $F_{e,\,s}$ pulls the droplet upwards, while $F_{e,\,p}$ pushes the droplet downwards. Also $F_{e,\,p}$ is proportional to the droplet base area, which in this case is smaller due to the high contact angle. As a result, the upward electrical forces exceed the downward force, manifesting a lift force.

In summary, it can be said that for the superhydrophobic droplet considered here, the primary influence of the electric field is a lifting of the droplet from the surface vertically and a net compression of the droplet radial (see Fig. 10b). It is worth noting that this induced lift force is related to the mechanism which is responsible for the droplet jumping phenomena observed for droplets on superhydrophobic surfaces in the presence of electric fields [41].

3.4. Heat transfer

Fig. 13 shows the time evolution of the droplet gas-liquid interface (a-b) and radial heat transfer (c-d) profiles for varied wetting and applied electric fields. Fig. 13 illustrates the impact of the electric field; each subplot consists of two data sets: non-electric field (left) and high electric field (right) at different points in time during their respective evaporation period. The geometric augmentation of the droplet morphology can be viewed by comparing the left (non-electric field) and right (high electric field) sides of Fig. 13a and b.

The pinned contact line CCR mode of evaporation of both hydrophilic cases is clearly visible for the t = 1, 5, and 9 min droplet profiles in Fig. 13a. Here, there is no notable change on the radial heat flux profile with respect to time or applied electric field (Fig. 13c). Once the contact line unpins, the receding contact line evaporation mode (t = 14 and 18 min) has associated with it a monotonic increase in the local heat flux over the entire base region, including the contact line, indicating an escalation in both the peak and average heat fluxes.

For the superhydrophobic case, the observations are quite different. Here, Fig. 13b shows that the shape change due to the applied electric field is more evident. However, consistent with the observation for the hydrophilic droplets subsequent to de-pinning, an increase in the local heat flux over the entire base region is observed for both superhydrophobic droplets as they evaporate with a receding contact line. Due to the reduction of the contact line radius by the applied electric field for t = 1, 8, 15, and 22 min, greater average and local maximum radial heat fluxes are noted for the electric field case in comparison with the non-electric field case over this time period. These thermal characteristics are further elucidated in Fig. 14.

Fig. 14. demonstrates the overall impact the electric field has on important time-varying heat transfer parameters: the power to the droplet, average heat flux, peak heat flux at the contact line, and base area. Results are shown for both the evaporating hydrophilic and superhydrophobic droplets considered in this work. For the hydrophilic droplets (Fig. 14a, c, e, and g), where the electric field does not significantly influence the heat flux distribution as discussed earlier, it is not surprising that both the droplets have similar magnitudes and trends for the total thermal power, average and peak heat flux across the solid-liquid boundary. A consistent initial power (t = 1 min, q = 63 mW) is noted for the non-

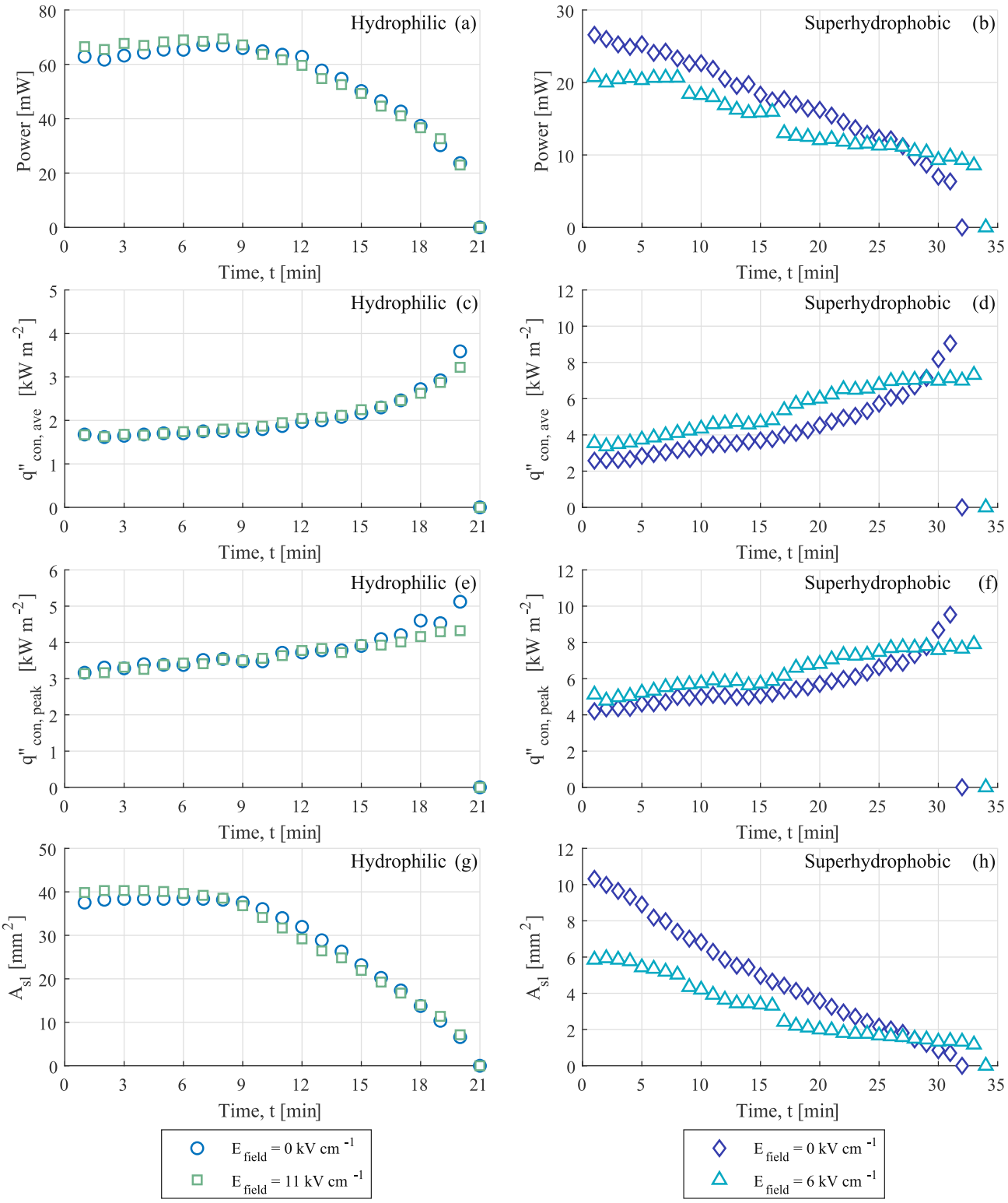

Fig. 14. Hydrophilic and superhydrophobic droplet heat transfer properties through time for varied applied electric field. (a-b) power, (c-d) average heat flux, (e-f) peak heat flux, and (g-h) solid-liquid base area.

electric field evaporation. This is marginally lower than the electric field case (q = 67 mW) likely due to the slightly larger overall solid-liquid surface area (A_{sl}) of the electric field case at t = 1 min which reduces the air-side thermal resistance. For a consistent base area in the CCR regime, a near-constant average heat flux and thermal power are noted for both cases. After the contact line unpins (t = 10-21 min), the receding contact line results in increasing average heat flux but with a decreasing thermal power, since the base area reduces. Overall, the net influence of the electric field on the heat transfer to the base of the hydrophilic droplet is small,

regardless of its noteworthy influence on the mechanics and morphology, and as a result, its influence on the evaporation rate is marginal (Fig. 7a).

For the superhydrophobic droplet (Figs. 14b, d, f, and h), a clear impact of the electric field is observed. Due to the combined action of the radial compressive force acting on it, and of the smaller contact angle hysteresis, the contact radius of the droplet in the electric field is comparatively smaller (Fig. 7d) than the field-free droplet for the preponderance of its evaporation period. As has been observed here as well as in the study of Gibbons et al. [1], reducing the base radius has the influence of increasing the local heat flux over the base of the droplet, including at the contact line region. This seems to be true regardless of whether the reduced base radius is caused by electric forces or due to the receding contact line during evaporation. Figs. 14d and f show the presence of the electric field has the predominant influence of increasing the average heat flux to the droplet in the presence of the electric field. However, this increase in the local and average heat flux is not sufficient to offset the reduced area of heat transfer at the base (Fig. 14h), so the net power to the droplet is, on the most part, reduced. This being the case, the total evaporation time is longer (Fig. 7b), though only marginally since there is positive tension between the reduced heat transfer area and the increase in base heat flux.

3.5. The Contact Line Density

Figs. 13c and d illustrate that when the base radius is large, the influence of the contact line heat transfer peak is confined to the region at the periphery of the droplet. Thus, this can be considered as a mixed-mode of heat transfer wherein the central and mid regions the heat transfer is diffusion/convection dominated (depending on the Peclet number), and the triple line is contact line dominated. However, when the base radius is small, the high transfer of the contact line dominates the heat transfer over the whole heat transfer area. Thus, in terms of the heat transfer mechanisms acting over the associated heat transfer area, the overall influence of the contact line is related to the length of the contact line compared with the overall area of heat transfer, i.e. if the length of the contact line increases in proportion to the base area of the droplet, then the heat transfer will become progressively more influenced by the high heat transfer associated with the contact line region.

A straight forward parameter, called the Contact Line Density (CLD) has been introduced [2,42] to quantify, in geometric terms, this relative proportion of the contact line on the overall base heat transfer region and is defined as,

$$\mathrm{CLD} = \frac{P_{CL}}{A_{sl}} \tag{11}$$

where P_{CL} is the perimeter of the triple line, and A_{sl} is the base area of the droplet. Since the droplets are axisymmetric, $P_{CL} = \pi D_b$ and $A_{sl} = 0.25 \cdot \pi {D_b}^2$, it follows that $CLD \propto {}^{1}/_{D_b}$. Therefore, contact line density and reciprocal base diameter are equivalent for the studied droplets, but CLD concept can be extended to non-axisymmetric cases, as verified e.g. in [42].

Fig. 15 compares the CLD of the evaporating droplets with the average heat flux across the solid-liquid interface for both wetting and electric field cases over their full evaporation periods. All of the data collapses onto a straight line that intersects the vertical axis at the applied heat flux (less minor losses), as it should [1]. These illustrate some potentially key insights about the CLD, the impact of the applied electric field, and the overall thermal resistance to heat transfer.

As previously reported [1,2], the CLD is the key parameter in terms of relating the average heat flux to the droplet dimensions

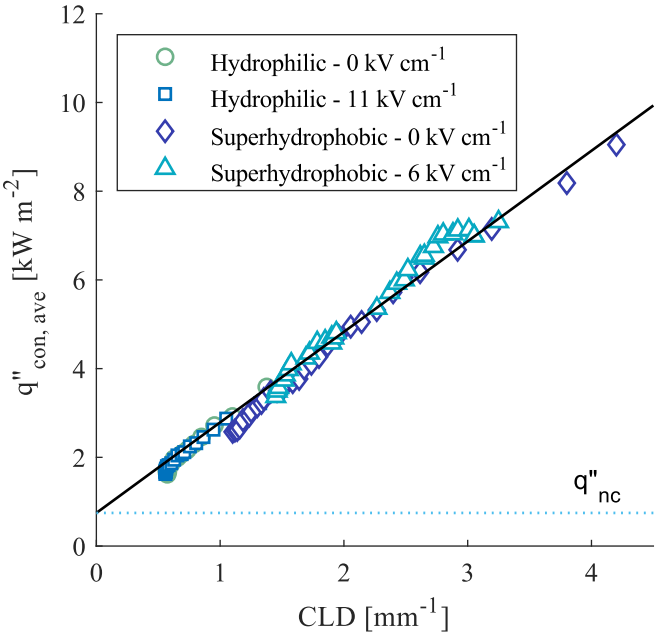

Fig. 15. Contact line density vs. average heat flux into the droplet base for varied wetting conditions and applied electric field.

since it takes into account the respective regions over which different heat transfer mechanisms act, i.e. diffusion/convection and contact line heat transfer. As the base radius decreases, the CLD increases, increasing the proportion of contact line heat transfer, thus causing the average heat flux to increase as well. As seen in Fig. 15 for the field-free droplets, and discussed previously by the current authors in [1], both the hydrophilic and superhydrophobic data collapse to a common straight line. This indicates that the overall thermal resistance is very strongly related to the size of the droplet base, which subsequently dictates the relative proportion of the mixed-mode heat transfer mechanisms.

When the droplets are subject to an electric field, the q'' - CLD relation provides an opportunity to interrogate the heat transfer in such a way as to determine if there is any notable augmentation in the heat transfer mechanisms specifically due to the EHD effect. If there were any additional enhancement or deterioration due to EHD, then one would expect a different the q'' - CLD relation compared with the field-free cases.

As Fig. 15 shows, the electric field data collapses onto the same line as that for the field-free cases. This is preliminary, yet convincing evidence to suggest that the main influencing factor of the electric field is related to its action on the droplet shape as it pertains to the contact line. The hydrophilic and superhydrophobic data presented here demonstrate that the electric field is an important parameter only if it significantly influences the droplet shape in such a way that it augments the contact line density of the evaporating droplet. If the electric field acts to change the CLD, a notable change in the heat transfer characteristics of the droplet is observed, and this is due to the shape augmentation and not specific EHD induced heat transfer enhancement.

From a practical point of view, this demonstrates some key points with regard to the application of droplets in two-phase heat transfer equipment such as those which implement spray cooling. Clearly, heat transfer will improve when a high density of small droplets impinge on the heated substrate, forming multiple individual evaporating sessile droplets with an overall high surface averaged CLD. Increasing the surface averaged CLD can be achieved

by decreasing the droplet size, increasing the surface hydrophobicity and implementation of electric fields.

4. Conclusions

The impact of an electric field on the evaporation of hydrophilic and superhydrophobic droplets has been investigated. To facilitate a deeper understanding of the problem, the heat flux distribution beneath the droplets as well as the droplet mechanics and resulting shapes and forces are contrasted for the entire evaporation period with and without the electric field. Both wetting scenarios show that the net radial directed electric force is directed inward, resulting in a compressive force which influences the droplet shape in such a way that it appears elongated. Conversely, the net vertically directed electric force is determined to be downwardly directed for hydrophilic droplets, pressing the droplet to the surface, whereas it is upwardly directed for the superhydrophobic droplets, representing a lifting force. With regard to the heat transfer to the droplets, only a pronounced electric field effect was observed for the superhydrophobic droplet. Examining the contact line density for all droplets demonstrates its unifying relationship with the average heat flux to the droplet. This result suggests that the electric field is an important parameter only if it significantly influences the droplet shape in such a way that it augments the contact line density of the evaporating droplet. If the electric field acts to change the CLD, a notable change in the heat transfer characteristics of the droplet is observed, and this is due to the shape augmentation and not specific EHD induced heat transfer enhancement. Future work will explore the impact of gravity on the heat transfer to evaporating hydrophobic and hydrophilic droplets. In tandem, the fluid motion within the droplet will be explored numerically and experimentally to further elucidate the present research to build a complete picture of the droplet evaporation phenomenon.

Declaration of Competing Interest

As far as I am aware, there are no current or potential conflicts of interest related to this work.

CRediT authorship contribution statement

M.J. Gibbons: Conceptualization, Methodology, Software, Data curation, Formal analysis, Validation, Visualization, Writing - original draft, Funding acquisition. **A.I. Garivalis:** Software, Formal analysis, Validation, Data curation, Writing - review & editing. **S. O'Shaughnessy:** Project administration, Resources, Writing - review & editing. **P. Di Marco:** Conceptualization, Supervision, Formal analysis, Writing - review & editing. **A.J. Robinson:** Conceptualization, Supervision, Writing - review & editing, Project administration, Funding acquisition.

Acknowledgements

The authors would like to acknowledge the financial support of the Irish Research Council under their Government of Ireland Postdoctoral Fellowship Programme, Grant No. IRC/GOIPD/2019/666.

Appendix A

For the present analysis, the leaky dielectric model, introduced by Melcher and Taylor [43] and later refined by Saville [44], was adopted for water. As pointed out by Jones [45] the conducting or insulating behaviour of a leaky dielectric is ruled by the comparison of the free charge relaxation time

$$\tau = \frac{\varepsilon_0 \varepsilon_R}{\sigma}$$

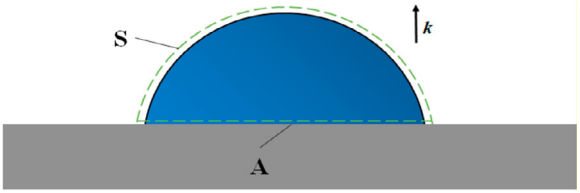

Fig. A1. Control volume surrounding the droplet.

with the characteristic time of the phenomenon. While the relative dielectric permittivity of water is well assessed, its conductivity σ is strongly dependent on contamination and can vary with time. In any case, it is quite difficult to get a relaxation time higher than 0.1 ms even with ultra-pure water. Therefore, water can be considered as an electric conductor in the present context, in which the evaporation time is in the order of minutes.

The numerical model was developed using the commercial software COMSOL Multiphysics. Electrostatics Module and 2D axisymmetric coordinates were chosen in order to exploit the droplet symmetry and reduce calculation time. The solver used was stationary, as the evaporation process quasi-static. The droplet profile obtained by shadowgraphy was imported in the model as an interpolating line. As the liquid has been considered a conductor, electric ground boundary condition was imposed at the gas-liquid interface, and the electric field resulted non-zero in the gas domain only.

The electric stresses and forces were calculated using the expressions of Maxwell's stress tensor $\boldsymbol{T_e}$ [40]. The explicit expression of the Maxwell's tensor components ($\sigma_{i,j}$) for a dielectric fluid is given:

$$\sigma_{i,j} = \varepsilon_0 \varepsilon_R E_i E_j - \frac{\varepsilon_0}{2} E^2 \left[\varepsilon_R - \rho \left(\frac{\partial \varepsilon_R}{\partial \rho} \right)_T \right] \delta_{i,j} \tag{12}$$

According to [40], considering the control volume surrounding the droplet as in Fig A1, the total electric force acting on the droplet can be considered the sum of three terms: $F_{e,S}$ acting on the liquid-vapour interface S, $F_{e,A}$, acting on the liquid-solid interface A, and $F_{e,p}$, which is the result of the internal pressure change induced by the surface modification.

$$F_{e,S} = \int_S \boldsymbol{k} \cdot \boldsymbol{T}_{e,v} \cdot \boldsymbol{n}_v dS \tag{13}$$

$$F_{e,A} = \int_A \boldsymbol{k} \cdot \boldsymbol{T}_{e,l} \cdot \boldsymbol{n}_l dA \tag{14}$$

$$F_{e,p} = -\frac{\pi {D_b}^2}{4} \Delta f_{e,n,0} = -\frac{\pi {D_b}^2}{4} \frac{\varepsilon_0 E_{v,0}^2}{2} \tag{15}$$

where $\Delta f_{e,n,0}$ is the electric stress difference at the interface calculated at the apex of the droplet, and D_b is the base diameter. In particular, in the considered case, the electric field is excluded from the liquid and $\boldsymbol{T}_{e,l} = F_{e,A} = 0$. Custom-made expression were implemented in COMSOL to evaluate the forces detailed above.

References

[1] M.J. Gibbons, P. Di Marco, A.J. Robinson, Heat flux distribution beneath evaporating hydrophilic and superhydrophobic droplets, Int. J. Heat Mass Transf. 148 (2020) 119093, doi:10.1016/j.ijheatmasstransfer.2019.119093.
[2] M.J. Gibbons, P. Di Marco, A.J. Robinson, Local heat transfer to an evaporating superhydrophobic droplet, Int. J. Heat Mass Transf. 121 (2018) 641–652, doi:10.1016/j.ijheatmasstransfer.2018.01.007.
[3] V.S. Ajaev, O.A. Kabov, Heat and mass transfer near contact lines on heated surfaces, Int. J. Heat Mass Transf. 108 (2017) 918–932.
[4] F. Carle, B. Sobac, D. Brutin, Experimental evidence of the atmospheric convective transport contribution to sessile droplet evaporation, Appl. Phys. Lett. (2013) 102, doi:10.1063/1.4792058.
[5] R.D. Deegan, O. Bakajin, T.F. Dupont, G. Huber, S.R. Nagel, T.A. Witten, Capillary flow as the cause of ring stains from dried liquid drops, Nature 389 (1997) 827–829, doi:10.1038/39827.

[6] B. Sobac, D. Brutin, Triple-line behavior and wettability controlled by nanocoated substrates: influence on sessile drop evaporation, Langmuir 27 (2011) 14999–15007.
[7] S. David, K. Sefiane, L. Tadrist, Experimental investigation of the effect of thermal properties of the substrate in the wetting and evaporation of sessile drops, Colloids Surfaces A Physicochem. Eng. Asp. 298 (2007) 108–114.
[8] P.A. Raghupathi, S.G. Kandlikar, Contact line region heat transfer mechanisms for an evaporating interface, Int. J. Heat Mass Transf. 95 (2016) 296–306.
[9] V. Vancauwenberghe, P. Di Marco, D. Brutin, Wetting and evaporation of a sessile drop under an external electrical field: A review, Colloids Surfaces A Physicochem. Eng. Asp. 432 (2013) 50–56.
[10] M.J. Gibbons, C.M. Howe, P. Di Marco, A.J. Robinson, Local Heat Transfer to an Evaporating Sessile Droplet in an Electric Field, J, Phys. Conf. Ser. 745 (2016) 032066, doi:10.1088/1742-6596/745/3/032066.
[11] I. Marchuk, A. Karchevsky, A. Surtaev, O. Kabov, Heat Flux at the Surface of Metal Foil Heater under Evaporating Sessile Droplets, Int. J. Aerosp. Eng. 2015 (2015).
[12] D. Brutin, Droplet Wetting and Evaporation: From Pure to Complex Fluids, Academic Press, 2015.
[13] P.A. Strizhak, R.S. Volkov, S.Y. Misyura, S.I. Lezhnin, V.S. Morozov, The role of convection in gas and liquid phases at droplet evaporation, Int. J. Therm. Sci. 134 (2018) 421–439, doi:10.1016/j.ijthermalsci.2018.08.031.
[14] H. Hu, R.G. Larson, Marangoni effect reverses coffee-ring depositions, J, Phys. Chem. B. 110 (2006) 7090–7094.
[15] S. Dash, S.V Garimella, Droplet evaporation dynamics on a superhydrophobic surface with negligible hysteresis, Langmuir (2013).
[16] M. Ait Saada, S. Chikh, L. Tadrist, Numerical investigation of heat and mass transfer of an evaporating sessile drop on a horizontal surface, Phys. Fluids. (2010) 22, doi:10.1063/1.3488676.
[17] M.K. Bologa, V.V. Pushkov, A.B. Berkov, Electric field induced heat transfer enhancement in a gas-solid suspension heat exchanger, Int. J. Heat Mass Transf. 28 (1985) 1245–1255, doi:10.1016/0017-9310(85)90156-5.
[18] E.R.G. Eckert, R.J. Goldstein, W.E. Ibele, S.V. Patankar, T.W. Simon, P.J. Strykowski, K.K. Tamma, T.H. Kuehn, A. Bar-Cohen, J.V.R. Heberlein, D.L. Hofeldt, K.A. Stelson, J.H. Davidson, Heat transfer - a review of 1993 literature, Int. J. Heat Mass Transf. 39 (1996) 885–963, doi:10.1016/0017-9310(95)00132-8.
[19] S. Di Bari, A.J. Robinson, Adiabatic bubble growth in uniform DC electric fields, Exp. Therm. Fluid Sci. 44 (2013) 114–123, doi:10.1016/j.expthermflusci.2012.06.004.
[20] M.J. Gibbons, A.J. Robinson, Electrospray array heat transfer, Int. J. Therm. Sci. 129 (2018) 451–461, doi:10.1016/j.ijthermalsci.2018.03.021.
[21] M.J. Gibbons, A.J. Robinson, Heat transfer characteristics of single cone-jet electrosprays, Int. J. Heat Mass Transf. 113 (2017) 70–83, doi:10.1016/j.ijheatmasstransfer.2017.04.119.
[22] Y. Liu, K. Oh, J.G. Bai, C.L. Chang, W. Yeo, J.H. Chung, K.H. Lee, W.K. Liu, Manipulation of nanoparticles and biomolecules by electric field and surface tension, Comput. Methods Appl. Mech. Eng. 197 (2008) 2156–2172, doi:10.1016/j.cma.2007.08.012.
[23] F. Mugele, J.C. Baret, Electrowetting: From basics to applications, J, Phys. Condens. Matter. (2005) 17, doi:10.1088/0953-8984/17/28/R01.
[24] S.A.O. Ahmedou, O. Rouaud, M. Havet, Assessment of the electrohydrodynamic drying process, Food Bioprocess Technol 2 (2009) 240–247, doi:10.1007/s11947-008-0078-6.
[25] P. Di Marco, R. Kurimoto, G. Saccone, K. Hayashi, A. Tomiyama, Bubble shape under the action of electric forces, Exp. Therm. Fluid Sci. 49 (2013) 160–168, doi:10.1016/j.expthermflusci.2013.04.015.
[26] R. Digilov, Charge-induced modification of contact angle: The secondary electrocapillary effect, Langmuir 16 (2000) 6719–6723, doi:10.1021/la991308a.
[27] A. Bateni, A. Ababneh, J.A.W. Elliott, A.W. Neumann, A. Amirfazli, Effect of gravity and electric field on shape and surface tension of drops, Adv. Sp. Res. 36 (2005) 64–69, doi:10.1016/j.asr.2005.02.084.
[28] A. Bateni, S. Laughton, H. Tavana, S.S. Susnar, A. Amirfazli, A.W. Neumann, Effect of electric fields on contact angle and surface tension of drops, J, Colloid Interface Sci 283 (2005) 215–222, doi:10.1016/j.jcis.2004.08.134.
[29] A. Bateni, S.S. Susnar, A. Amirfazli, A.W. Neumann, Development of a new methodology to study drop shape and surface tension in electric fields, Langmuir 20 (2004) 7589–7597, doi:10.1021/la0494167.
[30] P. Di Marco, N. Morganti, G. Saccone, Electric field effects on the dynamics of bubble detachment from an inclined surface, J, Phys. Conf. Ser. (2015) 655, doi:10.1088/1742-6596/655/1/012044.
[31] P. Di Marco, G. Saccone, Effects of Force Fields on Interface Dynamics, in view of Two-Phase Heat Transfer Enhancement and Phase Management for Space Applications, J, Phys. Conf. Ser. (2017) 923, doi:10.1088/1742-6596/923/1/012019.
[32] S. Siedel, S. Cioulachtjian, A.J. Robinson, J. Bonjour, Electric field effects during nucleate boiling from an artificial nucleation site, Exp. Therm. Fluid Sci. 35 (2011) 762–771, doi:10.1016/j.expthermflusci.2010.06.006.
[33] K. Takano, I. Tanasawa, S. Nishio, Enhancement of evaporation of a droplet from a hot surface by electric field, in: Int, Heat Transf. Conf. Digit. Libr., Begel House Inc (1990).
[34] K. Takano, I. Tanasawa, S. Nishio, Active enhancement of evaporation of a liquid drop on a hot solid surface using a static electric field, Int. J. Heat Mass Transf. 37 (1994) 65–71.
[35] K. Takano, I. Tanasawa, S. Nishio, Y. Hayata, Enhancement of Evaporation of a Droplet Using EHD Effect: Onset of Instability of Gas-Liquid Interface under Electric Field Applied in a Stepwise Manner, JSME Int. J. Ser. B Fluids Therm. Eng. 38 (1995) 288–294 http://www.mendeley.com/research/geology-volcanic-history-eruptive-style-yakedake-volcano-group-central-japan/.
[36] K. Takano, I. Tanasawa, S. Nishio, Enhancement of evaporation of a liquid droplet using EHD effect: criteria for instability of gas-liquid interface under electric field, J, Enhanc. Heat Transf. (1996) 3.
[37] H. Almohammadi, A. Amirfazli, Sessile drop evaporation under an electric field, Colloids Surfaces A Physicochem. Eng. Asp. 555 (2018) 580–585, doi:10.1016/j.colsurfa.2018.07.022.
[38] L. Kirkup, R.B. Frenkel, An Introduction to Uncertainty in Measurement, 2006. doi:10.1017/cbo9780511755538.
[39] S. Siedel, S. Cioulachtjian, A.J. Robinson, J. Bonjour, Integral momentum balance on a growing bubble, Phys. Fluids. 25 (2013) 123301.
[40] P. Di Marco, The use of electric force as a replacement of buoyancy in two-phase flow, Microgravity Sci. Technol. (2012), doi:10.1007/s12217-012-9312-y.
[41] K. Takeda, A. Nakajima, K. Hashimoto, T. Watanabe, Jump of water droplet from a super-hydrophobic film by vertical electric field, Surf. Sci. 519 (2002) 3–6, doi:10.1016/S0039-6028(02)02144-1.
[42] B. Horacek, K. Kiger, J. Kim, Single nozzle spray cooling heat transfer mechanisms, Int. J. Heat Mass Transf. 48 (2005) 1425–1438.
[43] J.R. Melcher, G.I. Taylor, Electrohydrodynamics: A Review of the Role of Interfacial Shear Stresses, Annu. Rev. Fluid Mech. (1969), doi:10.1146/annurev.fl.01.010169.000551.
[44] D.A. Saville, Electrohydrodynamics: The Taylor-Melcher Leaky Dielectric Model, Annu. Rev. Fluid Mech. (1997), doi:10.1146/annurev.fluid.29.1.27.
[45] T.B. Jones, Electrohydrodynamically Enhanced Heat Transfer in Liquids—A Review, Adv. Heat Transf. (1979), doi:10.1016/S0065-2717(08)70086-8.